remote sensing

MDPI

Technical Note

Experimental Co-Polarimetric GPR Survey on Artificial Vertical Concrete Cracks by the Improved Time-Varying Centroid Frequency Scheme

Xuebing Zhang [1,2], Junxuan Pei [1], Xianda Sha [1], Xuan Feng [2,*], Xin Hu [1,3], Changle Chen [2] and Zhengchun Song [1]

[1] School of Geomatics and Prospecting Engineering, Jilin Jianzhu University, Changchun 130118, China; zhangxuebing@jlju.edu.cn (X.Z.); shaxianda@student.jlju.edu.cn (X.S.); huxin@student.jlju.edu.cn (X.H.)
[2] College of Geo-Exploration Science and Technology, Jilin University, Changchun 130026, China
[3] Jiangxi Transportation Engineering Group Ltd., Nanchang 330038, China
* Correspondence: fengxuan@jlu.edu.cn; Tel.: +86-13404353645

Abstract: The experimental setup is devised to simulate the presence of vertical cracks with varying widths within concrete structures. Co-polarimetric ground-penetrating radar (GPR) surveys are carried out to acquire the "VV" and "HH" polarization data. The time-varying centroid frequency attribute is employed to describe the vertical variation in the center frequency of the radar wave, unveiling a gradual vertical decay in the centroid frequency at the locations of vertical cracks. An improved time-varying centroid frequency attribute based on the adaptive sparse S-transform (ASST) is proposed and tested by a finite-difference time-domain model and co-polarimetric GPR data, which can offer better resolution compared to that of the conventional S-transform. By analyzing the waveform and centroid frequency properties of the two polarizations, we conclude that the "VV" polarization is relatively sensitive to centimeter scale cracks, while the "HH" polarization is more sensitive to millimeter scale cracks.

Keywords: ground-penetrating radar (GPR); co-polarimetric; improved time-varying centroid frequency; void analysis; adaptive sparse S-transform (ASST)

check for updates

Citation: Zhang, X.; Pei, J.; Sha, X.; Feng, X.; Hu, X.; Chen, C.; Song, Z. Experimental Co-Polarimetric GPR Survey on Artificial Vertical Concrete Cracks by the Improved Time-Varying Centroid Frequency Scheme. *Remote Sens.* **2024**, *16*, 2095. https://doi.org/10.3390/rs16122095

Academic Editors: Joan Ramon Casas Rius, Necati Catbas, Rolando A. Chacón and Daniele Zonta

Received: 22 April 2024
Revised: 5 June 2024
Accepted: 7 June 2024
Published: 10 June 2024

Copyright: © 2024 by the authors. Licensee MDPI, Basel, Switzerland. This article is an open access article distributed under the terms and conditions of the Creative Commons Attribution (CC BY) license (https://creativecommons.org/licenses/by/4.0/).

1. Introduction

Ground-penetrating radar (GPR) is a vital technique in near-surface geophysics, used for identifying subsurface targets and conducting field surveys [1,2] through the transmission and reception of high-frequency electromagnetic waves [3]. In recent years, GPR has been widely applied in civil engineering, including evaluating concrete curing effects [4,5], assessing moisture content of building materials [6], conducting diagnostic testing of specific building structures [7–9] and detecting damage in heritage buildings [10,11]. Among these applications, the presence and development of cracks or voids can occur in various environments, such as buildings [12] and road and pavement [13–16], and become significant concerns in civil engineering. The digital image correlation (DIC) technique [17] can be utilized to identify surface cracks, while drill core sampling is employed for analyzing internal cracks within structures. Accurate extraction and analysis of internal cracks are often necessary for research purposes. Although core drilling sampling technology is more established, it has evident drawbacks in terms of destructiveness and irreversibility. In such cases, utilizing non-destructive testing methods like GPR would be a more prudent choice.

The resolution and detection depth of GPR are closely tied to the center frequency of the selected transmitting antenna. Mainstream GPR radar products typically operate within a frequency range from 10 MHz to 3 GHz, corresponding to electromagnetic field wavelengths ranging from approximately 0.3 m to 10 m in general low-loss media (calculated with a velocity of 10 cm/ns). In GPR B-scan profiles, large target bodies such as

metal pipes and road voids can be clearly identified through waveform patterns or events, including hyperbolic reflections and multiples. However, the sensitivity of waveform responses to smaller targets is significantly lower, posing challenges in detecting target bodies or abnormalities smaller than one wavelength in size.

A fundamental approach for detecting minor abnormalities involves examining not only waveforms but also the corresponding time–frequency characteristics and their size-dependent alterations [18,19]. Traditional time–frequency transforms, such as short-time Fourier transform (STFT), wavelet transform and S-transform [20–23], are commonly employed for this purpose. Recently, sparse time–frequency analysis has gained prominence as a highly efficient method. In comparison to the conventional S-transform, the adaptive sparse S-transform (ASST) [24] offers superior resolution for non-stationary signal analysis due to its adaptive window function. In this work, the GPR data acquired above cracks are processed using the ASST instead of the classic S-transform to derive a 2D energy distribution for each A-scan in the time–frequency plane. However, analyzing the time–frequency spectrum A-scan by A-scan may not be intuitive. Therefore, we further compact the derived ASST-based time–frequency spectrum and extract the corresponding time-varying centroid frequency (CF) attribute [23,25] for each A-scan to obtain the centroid frequency profile, allowing for tracking changes in dominant frequency with spreading time in B-scan and benefiting the final crack interpretation.

In addition, commercial GPR devices such as the GSSI SIR series and MALÅ HDR series commonly employ single-polarization systems consisting of two shielded bow-tie antennas arranged in parallel. The transmitting antenna emits wide-band and linearly polarized electromagnetic waves, while the receiving antenna captures the response from subsurface target objects. This polarization mode is usually referred to as "VV", where "V" represents vertical linear polarization in the X-Y plane. However, subsurface targets have the ability to modify the polarization of the scattered wave, resulting in a different polarization compared to that of the incident wave. Therefore, relying solely on single-polarization profiles may not provide sufficient accuracy and comprehensiveness for the analysis of underground targets. Therefore, it is essential to consider the impact of polarization. In recent years, several full-polarimetric ground-penetrating radar (FP-GPR) systems [26,27] have been developed and demonstrated their effectiveness in subsurface imaging and fracture characterization [28–31]. In addition to collecting "VV" data, these FP-GPR systems also acquire "HH" and "HV" data, where "H" represents horizontal linear polarization. The co-polarimetric data include both "VV" and "HH," while the cross-polarization data refers to the "HV" measurements. However, achieving FP-GPR data is challenging for most commercial GPR devices.

In this study, we first placed a set of plain concrete slats in parallel and covered them with polystyrene sheets to replicate internal cracks of varying sizes within the concrete structure. Considering the spatial orientation of the radar antenna relative to the cracks, we conducted co-polarimetric GPR surveys to acquire "VV" and "HH" polarization data. Subsequently, we developed an improved time-varying centroid frequency scheme based on ASST and applied it to the collected co-polarization GPR data in order to track the time–frequency characteristics of crack changes associated with crack width. This enables us to provide a more rational explanation for extracting and identifying crack information.

2. Methods

2.1. Adaptive Sparse S-transform (ASST)

The conventional S-transform, pioneered by Stockwell in 1996 [20], is capable of characterizing the time–frequency distribution of the time series as

$$S(\tau, f) = \int_{-\infty}^{\infty} x(t) \frac{|f|}{\sqrt{2\pi}} e^{-\frac{(\tau-t)^2 f^2}{2}} e^{-i2\pi f t} dt \quad (1)$$

where f denotes the frequency and $i^2 = -1$. τ represents the time-shift parameter which controls the position of the Gaussian window on the t-axis.

By introducing the constraint of sparsity, Sattari [24] proposed a sparsity-based adaptive time–frequency transform, known as "the adaptive sparse S-transform", which is defined as follows:

$$tfr(f,\tau) = \int_{-\infty}^{+\infty} \hat{x}(f+\alpha) e^{-\frac{2\pi\alpha^2}{f^2}} e^{i2\pi\alpha\tau} d\alpha \tag{2}$$

where α is the frequency shift and $\hat{x}(f)$ is the Fourier transform of $x(t)$. The algorithm also necessitates the optimization of window parameters [21,32] to accommodate abrupt changes in non-stationary signals:

$$\mathrm{TFR}_{ST}^{[l]}[l,k] = \mathrm{IFT}\left\{ \mathbf{A}_{s[m]}[l,m] \bigodot \hat{\mathbf{X}}[l,m] \right\} \tag{3}$$

where $\mathbf{A}_{s[m]}[l,m] \in \mathrm{R}^{\mathrm{N}\times\mathrm{N}}$ is the desired matrix of an adaptive window with shifted arbitrary windows, its column form is $\mathbf{a}^{s[m]}[m+l-1]$, standard windows on its rows, $\hat{\mathbf{X}}[l,m] \in \mathrm{C}^{\mathrm{N}\times\mathrm{N}}$ is the repetition of $\hat{\mathbf{x}}[l]$ for a total of m instances, and the operator $\bigodot$ denotes the sample-by-sample multiplication of two matrices [24].

2.2. Improved Centroid Frequency Based on the ASST

The original time-varying centroid frequency attribute can be expressed as

$$f_c(t) = \frac{\int_0^\infty f S(t,f) df}{\int_0^\infty S(t,f) df} \tag{4}$$

where $S(t,f)$ denotes the time–frequency spectrum derived by the S-transform.

When we utilize the ASST instead of the conventional S-transform to obtain the corresponding time–frequency distribution $tfr(t,f)$, the improved time-varying centroid frequency scheme can be represented as

$$\widetilde{f}_c(t) = \frac{\int_0^\infty f tfr(t,f) df}{\int_0^\infty tfr(t,f) df} \tag{5}$$

The centroid frequency, from a "wavelet" perspective, can be considered as an approximation of the time-varying dominant frequency (or most energetic frequency) of the wavelets [33,34]. To evaluate the effectiveness of the proposed time-varying centroid frequency scheme in depicting changes in dominant frequency, we constructed a two-layer model (2.5 m × 0.8 m) with an inclined interface for numerical simulation using the finite-difference in time domain (FDTD); see Figure 1a. The first layer (concrete) is modeled based on the stochastic media theory [35] to better represent the real situation of concrete, with a relative permittivity of around 4~6 and a conductivity set at 0.01. The bottom layer consists of wet sand, with a relative permittivity and conductivity set at 18 and 0.1 respectively. The transmitting and receiving antenna are denoted by the green and red blocks on the field surface. We adopt a 1.2 GHz Ricker source, and the offset is 0.08 m. The resulting B-scan obtained from FDTD simulation is presented in Figure 1b, where both direct wave and reflective waves from the inclined interface are visible at the top and middle sections of the B-scan.

The attribute profiles of conventional centroid frequency and the proposed ASST-based centroid frequency scheme are presented in Figure 1c,d, respectively. In both attribute profiles, the centroid frequency of direct waves and reflections from the inclined interface are clearly observable and distributed around the center frequency of the source wavelet, while the energy for reflective waves in the B-scan undergoes more attenuation than that of the direct waves. The subsurface layers can be more easily identified in the centroid frequency profiles using the proposed ASST-based scheme, as shown in Figure 1d, which exhibits better resolution. This is evident from the clearer depiction of scatter introduced by stochastic media and multiples at the bottom, as indicated by the black arrows. Additionally,

the proposed scheme allows for observation of the obvious decay [36] in centroid frequency of the multiple, demonstrating its superior resolution compared to conventional methods.

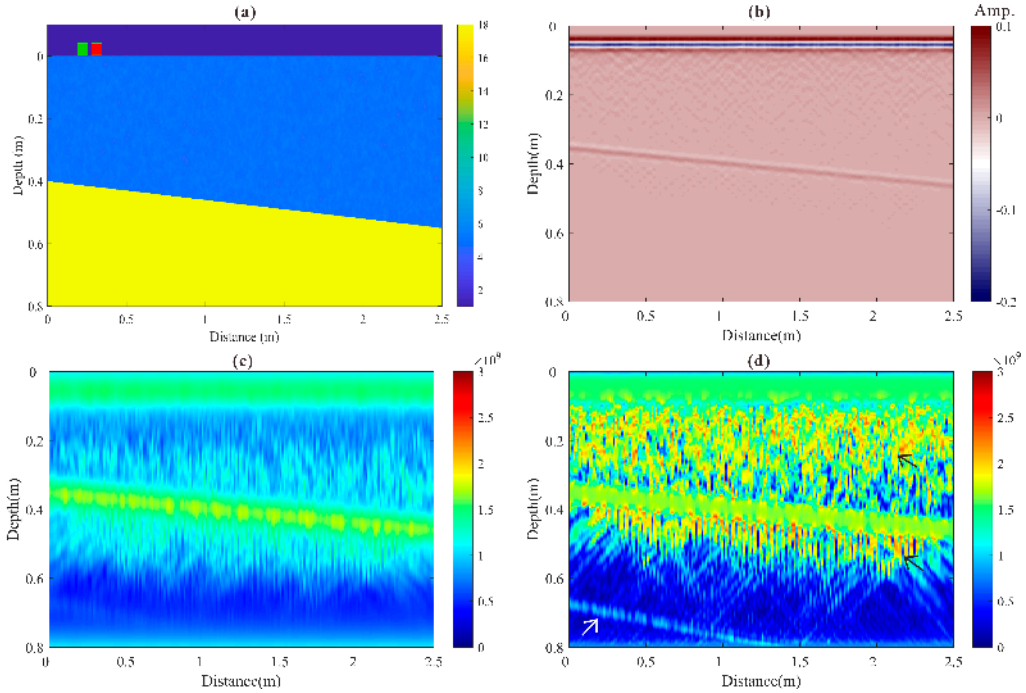


Figure 1. (**a**) The relative permittivity model of the two-layer simple model with an inclined interface (**a**), the derived B−scan by using the FDTD simulation (**b**); (**c**,**d**) correspond to the attribute profiles derived by the conventional centroid frequency scheme and the proposed ASST−based centroid frequency scheme, respectively.

3. Results

3.1. Experimental Setup and Co-Polarimetric GPR Data Acquisitions

We established an experimental setup to replicate the real-life occurrence of small cracks of varying sizes in highway roads or concrete structures, as described in reference [18]. Initially, a series of plain concrete beams or slats (10 cm width × 15 cm height) was arranged with contacts in parallel (see Figure 2a). The surface of the concrete slats exhibits a high degree of roughness, which may result in numerous discontinuities if the GPR vehicle collects data directly from it, thereby impacting data continuity. Therefore, a 5 cm thick layer of polystyrene plate was applied to cover these beams prior to subsequent GPR data acquisitions as depicted in Figure 2b. This experimental setup also holds some practical significance, such as for insulation layers on the exterior of buildings [37,38]. The concrete beams were displaced from the center at various distances, specifically 6 cm, 3 cm, 2 cm and 1 cm crack widths, to simulate internal vertical cracks within the concrete structure (see Figure 2c,d,e).

We conducted data acquisitions using a GPR system equipped with a GSSI 1.6 GHz antenna, corresponding to a wavelength of approximately 8 cm in concrete media. The experimental design aimed to detect cracks smaller than one wavelength in size. The crack widths for the first four groups correspond to approximately 3/4 wavelength, 3/8 wavelength, 1/4 wavelength and 1/8 wavelength. Additionally, we included a control group with a crack width of 0 cm as a reference and took measures to avoid alignment errors during displacement.

The survey lines were positioned along the central axis of the polystyrene plate, marked by a black marker (see Figure 3a). The acquisition mode utilized was the "ranging mode", which uses the wheel to determine the distance traveled along the survey line. The time window was fixed at 5 ns, and the sampling frequency was 20 GHz. Taking into account antenna polarization effects, measurements were conducted using both "VV" and

"HH" polarization, with the antenna dipole parallel and perpendicular to the measurement line, respectively (refer to Figure 3b,c).

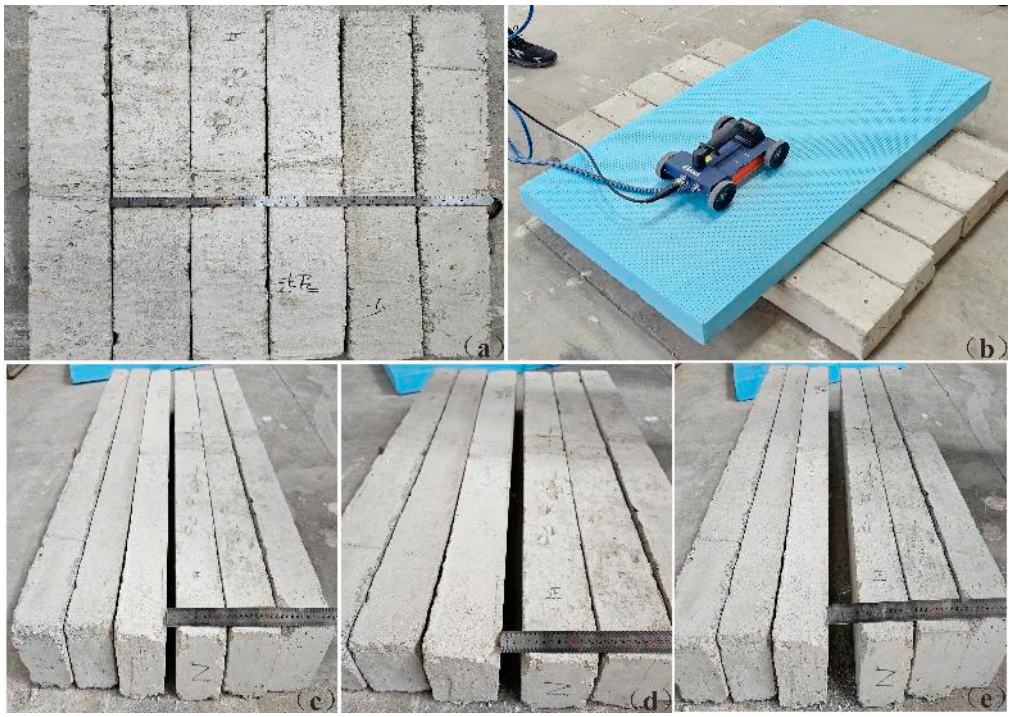


Figure 2. Experimental setup: (**a**) a series of plain concrete slats (120 cm × 10 cm × 15 cm) were arranged in parallel, (**b**) GPR system with a GSSI 1.6 GHz antenna, and field test diagrams for crack widths of (**c**) 2 cm, (**d**) 3 cm and (**e**) 6 cm.

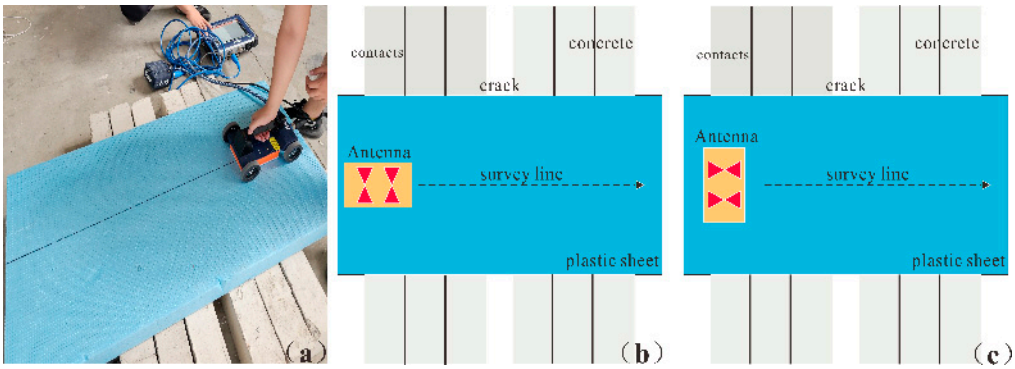


Figure 3. (**a**) Co-polarimetric GPR data acquisitions, (**b**) the "VV" mode, i.e., GPR acquisitions with the antenna dipoles perpendicular to the survey line (parallel to the crack) and (**c**) the "HH" mode, i.e., GPR acquisitions with the antenna dipoles parallel to the survey line (perpendicular to the crack).

3.2. Basic Signal Processing and Analysis

We acquired a total of ten sets of GPR B-scan data. We conducted initial signal processing steps including global background and DC removal, FIR band-pass filtering, AGC gain and deconvolution. The processed B-scans are exhibited in Figure 4. The B-scan profiles in Figure 4a,c,e,g,i were obtained using "VV" polarization from the concrete member with crack widths of 6 cm, 3 cm, 2 cm, 1 cm and 0 cm, respectively. Similarly, the B-scan in Figure 4b,d,f,h,j were collected using "HH" polarization. The interfaces between the plain concrete beams and the polystyrene plate above are indicated by blue dashed lines, while the lower interface is indicated by red dashed lines.

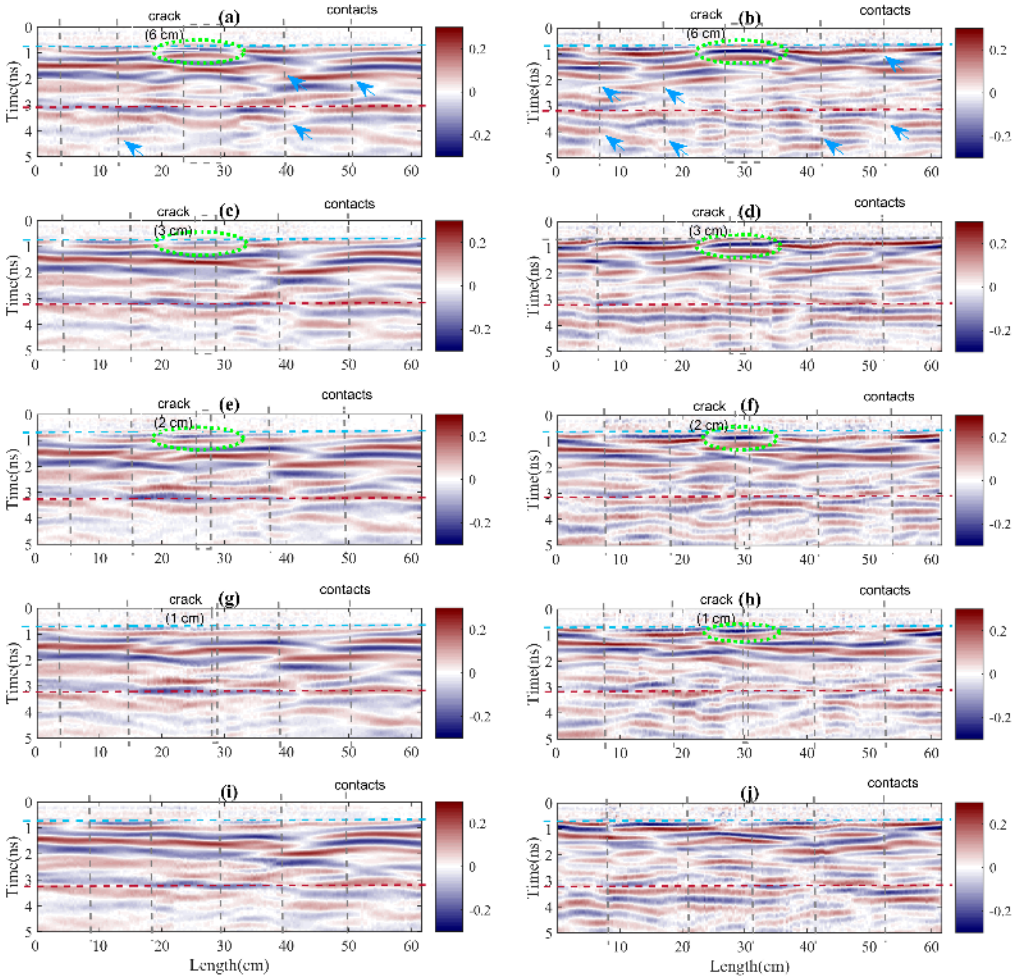


Figure 4. The B−scan profiles after initial signal processing. (**a**,**c**,**e**,**g**,**i**) were obtained using "VV" polarization from the concrete member with crack widths of 6 cm, 3 cm, 2 cm, 1 cm and 0 cm, respectively. Similarly, (**b**,**d**,**f**,**h**,**j**) were collected using "HH" polarization. The interfaces between the plain concrete beams and the polystyrene plate above are marked by blue dashed lines, while the lower interface is indicated by red dashed lines. Cracks and contacts are identified by dashed boxes and lines. The hyperbolic anomalies corresponding to the cracks are indicated by green ellipses.

The cracks of varying widths and the contacts are indicated using gray dashed boxes and lines. The hyperbolic anomalies corresponding to the cracks (indicated by green ellipses) can be identified in both "VV" and "HH" polarizations, with the latter acquisition scheme emphasizing the anomalies more prominently. In the case of the thinnest crack (i.e., 1 cm), the hyperbolic anomaly is visible only in "HH" polarization, while it is not observable in the "VV" profile.

The contacts between concrete slats can be seen as millimeter scale cracks [39,40]. In the B-scan profiles for both polarizations, the response to millimeter scale cracks at the contact points can also be observed, resulting in discontinuous reflections. These discontinuities due to the contacts are indicated by blue arrows in the 6 cm width profiles. The "VV" polarization profiles (see left column of Figure 4) show greater continuity in the reflections, suggesting a less sensitive response to contacts. In contrast, the "HH" polarization profiles exhibit a more pronounced response to contacts, making it more suitable for detecting cracks perpendicular to the survey line [30,41].

In addition, the "VV" profiles exhibit significantly fewer instances of scattering and multiple reflections compared to the "HH" profiles. As a result, the interfaces between the plain concrete slabs and the polystyrene plate above, as well as the lower interface, can be

clearly distinguished primarily based on the "VV" profiles. We represent both interfaces on all profiles using blue and red dashed lines.

Based solely on the results of the waveform analysis above, it is not sufficiently comprehensive for evaluating and analyzing cracks and contacts in the concrete member. In the following section, further discussion will be conducted to assess the proposed ASST-based centroid frequency attribute in GPR civil interpretation.

3.3. Improved Centroid Frequency Attribute Profiles

In this section, we further employ the improved centroid frequency based on adaptive sparse S-transform for co-polarization analysis of vertical cracks with varying widths, as depicted in Figure 5. Figure 5a,c,e,g,i depict the time-varying centroid frequency attribute profiles of the "VV" polarization B-scans corresponding to crack widths of 6 cm, 3 cm, 2 cm, 1 cm and 0 cm, respectively. Similarly, the corresponding time-varying centroid frequency attribute profiles for "HH" polarization B-scans are shown in Figure 5b,d,f,h,j. Refer to Figure 4, where the interfaces between the plain concrete slats and the polystyrene plate as well as the lower interface can also be identified from the centroid frequency profiles for both polarization, which are also marked by blue and red dashed lines, respectively.

The majority of the high-centroid frequency components (approximately 1.6~2.2 GHz) in the attribute profiles for both polarizations are concentrated in the shallow part. As the spreading time of the radar wave increases, there is a noticeable decrease in centroid frequency due to the attenuation effect (i.e., dielectric losses). This decrease is more pronounced in the attribute profiles of the "VV" polarization.

It is noteworthy that the centroid frequency at the cracks decays much more slowly than other parts in the "VV" profiles, as indicated by the dashed ellipses in Figure 5a,c,e,g. The lateral contrast may be attributed to the lower dielectric losses experienced by high-frequency electromagnetic waves propagating through air in the cracks compared to propagation in concrete. This contrast is particularly noticeable in the "VV" attribute profiles, as the backscattering width for high-impedance dielectric target bodies in the "VV" polarization is smaller than that of the "HH" polarization for air cracks [42], making contacts almost invisible and only allowing thicker vertical cracks to be seen. This phenomenon can be utilized for vertical crack identification.

The backscattering width in the "HH" centroid frequency attribute profiles exceeds that of the "VV" polarization, allowing for a more comprehensive observation of the response to contacts. The decrease in centroid frequency can also be detected, enabling the identification of contacts based on lateral discontinuity of centroid frequency, as shown in Figure 5j. This is due to the sensitivity of "HH" polarization to millimeter scale cracks as discussed in Section 3.2, which is also reflected in the "HH" centroid frequency profiles. At the locations of thicker cracks, although there is also a gradual decrease in centroid frequency (e.g., 6 cm, 3 cm; see dashed ellipses in Figure 5b,d), the lateral contrast mentioned above is not sufficiently pronounced to clearly indicate the presence of cracks. As for the case of thinner cracks (i.e., Figure 5f,h), the lateral contrast becomes less obvious.

For comparison, we also derive the centroid frequency profiles based on the conventional S-transform as shown in Figure 6. Figure 6a,c,e,g,i depict the derived time-varying centroid frequency attribute profiles of the "VV" polarization B-scans corresponding to varying crack widths (i.e., 6 cm, 3 cm, 2 cm, 1 cm and 0 cm), while the attribute profiles for "HH" polarization are shown in Figure 6b,d,f,h,j. Similar to Figure 5, the upper and lower interfaces are also marked by blue and red dashed lines, with cracks and contacts depicted by the dashed boxes and lines.

The overall distribution of centroid frequency components is generally consistent with that in Figure 5, although the resolution is lower. The lateral contrast of centroid frequency due to the vertical slow decay at the cracks can also be observed in the "VV" polarization, as shown by the dashed ellipses in Figure 6a,c,e,g, but cannot be identified in attribute profiles for "HH" polarization due to its low resolution. For a more detailed comparison, we also performed magnified imaging (zooming) on the centroid frequency profiles corre-

sponding to the slats with and without cracks. In this instance, we will utilize the "VV" profiles (Figure 5a,i and Figure 6a,i) as an illustration; see Figure 7. Figure 7a,c depict the magnified centroid frequency components located at a significant distance from the crack (approximately 16–19 cm) and above the crack (22–32 cm), in accordance with the proposed scheme. They demonstrate superior resolution compared to the conventional S-transform (Figure 7b,d), as indicated by the red circles. Furthermore, Figure 7c illustrates the gradual decrease in centroid frequency components using the proposed scheme (highlighted by square box in Figure 7c) with improved resolution, while also highlighting the lowest points of crack with black arrows. In the "VV" acquisition without cracks, the proposed scheme (Figure 7e,g) also demonstrates higher resolution compared to Figure 7f,h, with no observed gradual decrease in centroid frequency.

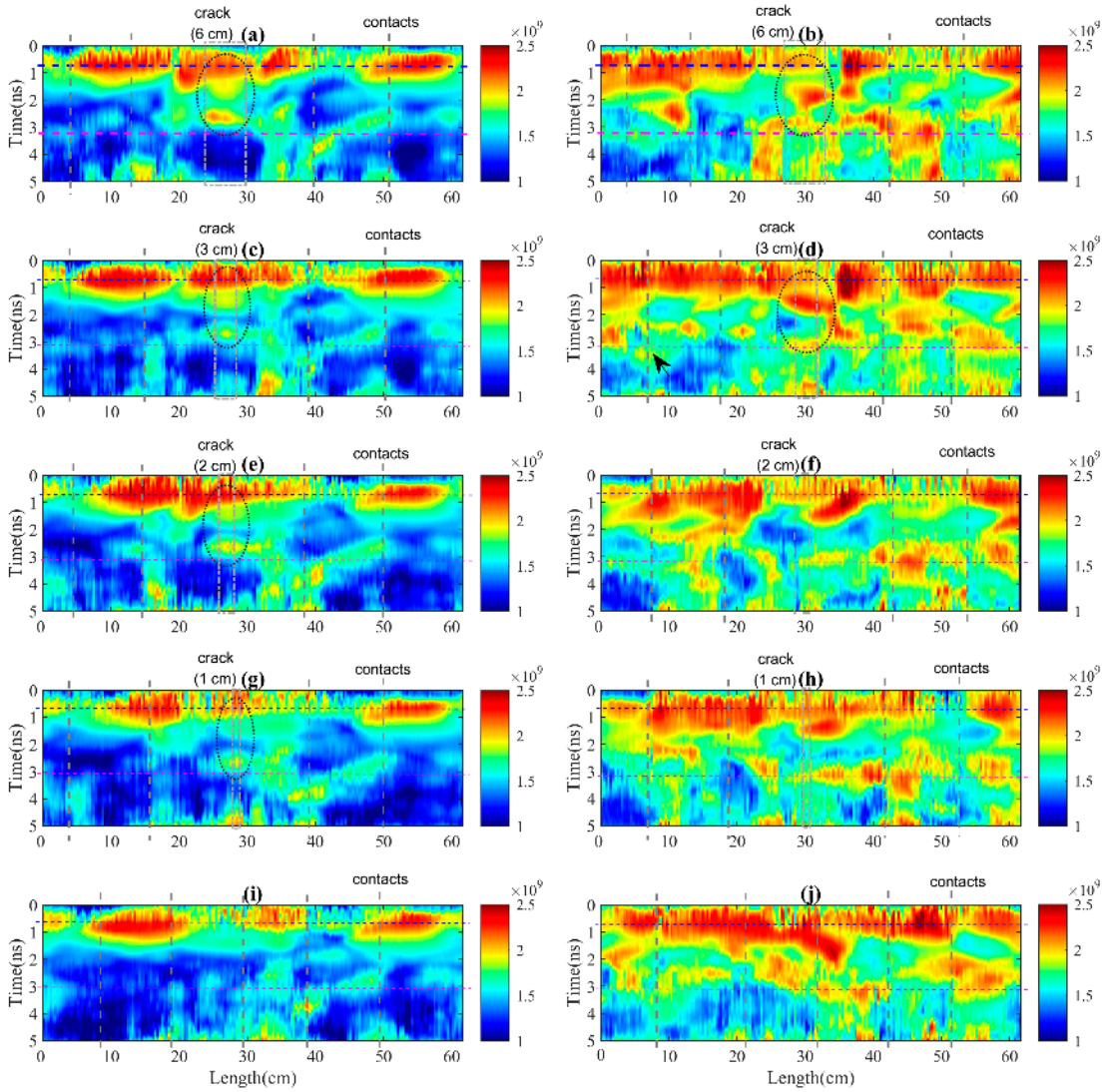


Figure 5. The proposed ASST-based time-varying centroid frequency attribute profiles of the co-polarimetric GPR data. (**a**,**c**,**e**,**g**,**i**) depict the derived attribute profiles for "VV" polarization corresponding to crack widths of 6 cm, 3 cm, 2 cm, 1 cm and 0 cm, respectively. Similarly, the attribute profiles for "HH" polarization are shown in (**b**,**d**,**f**,**h**,**j**). The upper and lower interfaces are marked by blue and red dashed lines. Cracks and contacts are identified by dashed boxes and lines.

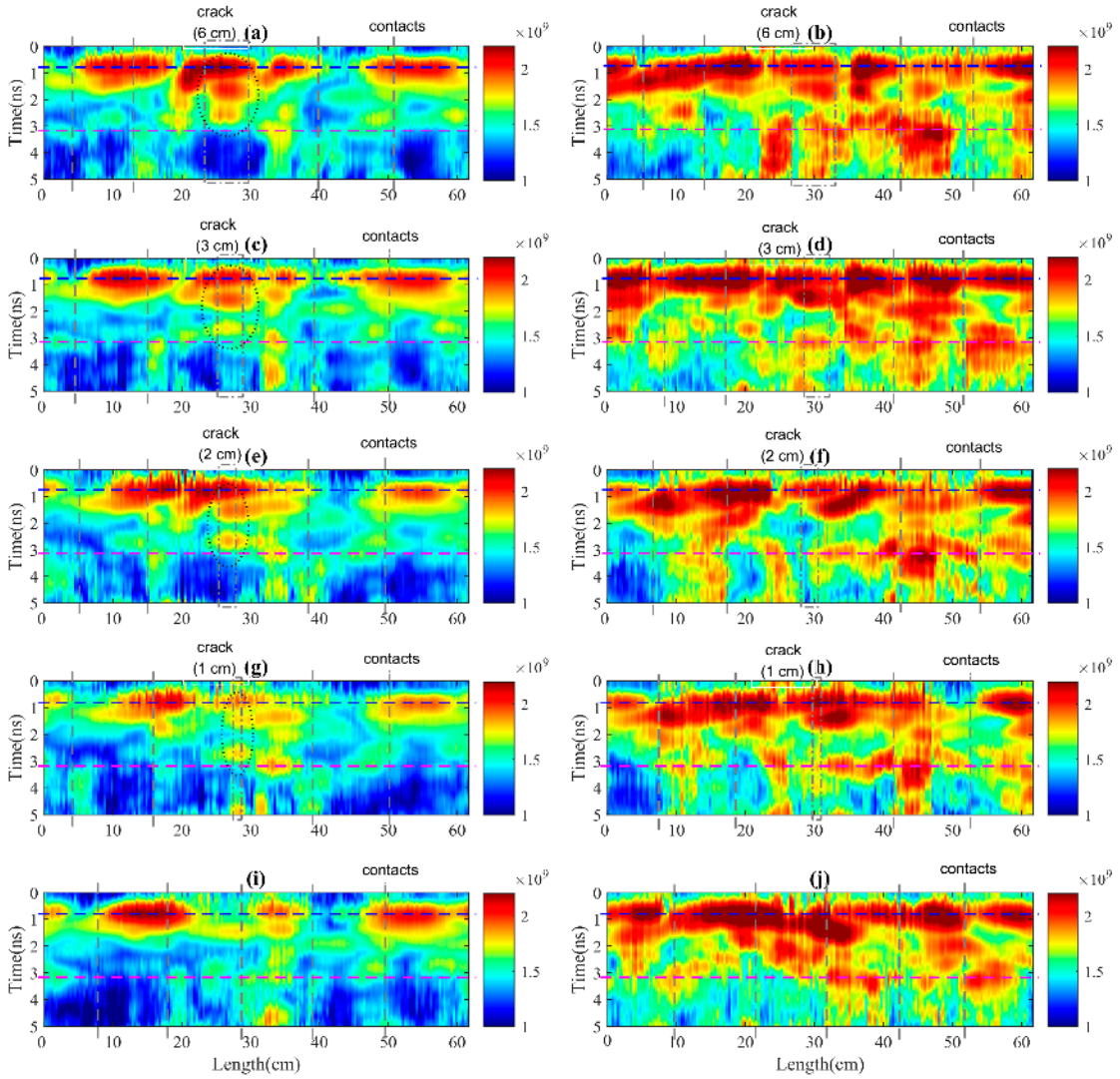


Figure 6. The S-transform-based time-varying centroid frequency attribute profiles of the co-polarimetric GPR data. (**a**,**c**,**e**,**g**,**i**) depict the derived attribute profiles for the "VV" polarization corresponding to crack widths of 6 cm, 3 cm, 2 cm, 1 cm and 0 cm, respectively. Similarly, the corresponding attribute profiles for "HH" polarization are shown in (**b**,**d**,**f**,**h**,**j**). The upper and lower interfaces are also marked by blue and red dashed lines, with cracks and contacts identified by dashed boxes and lines.

Through the above analysis, it can be concluded that the centroid frequency attribute profiles for "VV" polarization reveal the lateral contrast due to a gradual decrease, and can be leveraged for vertical crack identification, while the attribute profiles for "HH" polarization are more sensitive to the lateral discontinuity of centroid frequency which can be used to identify the boundary of contacts.

After conducting the aforementioned analysis, it can be deduced that the proposed centroid frequency attribute profiles for "VV" polarization exhibit lateral contrast due to a gradual decrease in centroid frequency, thereby facilitating vertical crack identification. Conversely, the attribute profiles for "HH" polarization demonstrate heightened lateral sensitivity towards discontinuity, enabling effective identification of contact boundaries. Moreover, compared with the centroid frequency attribute profiles based on the conventional S-transform, the proposed scheme exhibits better resolution.

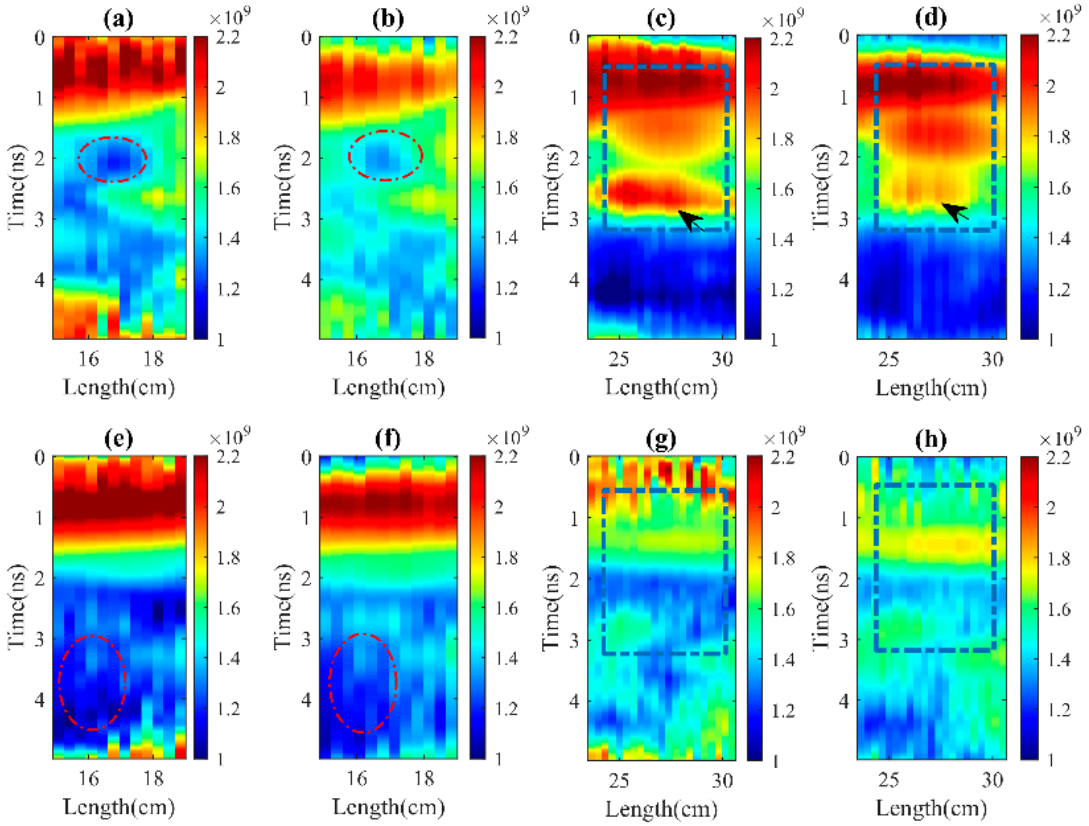


Figure 7. The magnified imaging (zooming) of "VV" centroid frequency profiles corresponding to the slats with and without cracks. For the slats with cracks, (**a**,**c**) are the zoomed centroid frequency components located at a significant distance from the crack (approximately 16–19 cm) and above the crack (22–32 cm), in accordance with the proposed scheme, while (**b**,**d**) are that of the conventional S-transform. Notably, (**c**) demonstrates a gradual decrease in centroid frequency with improved resolution compared to (**d**), and the bottom of the crack is more distinctly pointed. Meanwhile, zoomed centroid frequency components (**e**,**f**,**g**,**h**) for the case of no crack provide a basis for comparison.

4. Discussion

In this study, we perform the co-polarimetric GPR surveys for deriving the "VV" and "HH" polarization data. In the "VV" polarization (the transmitting and receiving bow-tie antenna oriented parallel to the cracks), the response to the millimeter scale cracks (e.g., the contacts in this setup) is less sensitive than that of "HH" polarization (the transmitting and receiving bow-tie antenna oriented orthogonal to the cracks). This is because the millimeter scale cracks can be viewed as high-impedance dielectric abnormalities, and the corresponding backscattering widths of the "HH" polarization are greater than that of the "VV" polarization [42]. This feature is also reflected in the proposed centroid frequency attribute profiles. Conversely, for isolated cracks with greater thickness or size (e.g., the crack with a width of 6 cm), the "VV" polarization may be a better choice as it is less sensitive to minor contacts which can be seen as interference.

The polarization analysis of co-polarimetric data alone is not sufficiently comprehensive for evaluating and analyzing cracks. We have attempted to utilize the time-varying centroid frequency attribute to depict the vertical variation of radar wave center frequency and have observed a gradual vertical decay in centroid frequency at locations of vertical cracks. This could be attributed to the fact that high-frequency electromagnetic waves propagating through cracks (air) experience lower dielectric losses compared to propagation in general lossy media. This phenomenon can also be leveraged for vertical crack identification, with the contrast being particularly prominent in the "VV" attribute profiles.

With the introduction of ASST, the improved centroid frequency scheme provides better resolution than that based on the conventional S-transform.

Furthermore, in order to simulate internal cracks of varying sizes in the concrete member, we utilized an experimental setup consisting of a series of plain concrete slabs arranged in parallel and covered with polystyrene sheets. However, actual cracks often exhibit irregularities and are characterized by randomness. It is important to consider more random shapes in order to better replicate real-world conditions as well as the corresponding scattering mechanism of actual cracks. Additionally, our current study only considered co-polarization GPR surveying and did not include cross-polarization measurement methods. In subsequent work, we will incorporate full-polarization measurement methods and consider an experimental scheme that closely resembles actual crack patterns for crack property identification analysis.

5. Conclusions

This study presents an experimental setup to simulate the presence of vertical cracks with varying widths within concrete structures or highway roadways. Co-polarimetric GPR surveys are conducted to obtain "VV" and "HH" polarization data. The time-varying centroid frequency attribute is applied to describe the vertical variation of the center frequency of radar wave, revealing a gradual vertical decay in centroid frequency at locations of vertical cracks. An improved time-varying centroid frequency attribute based on the ASST is proposed, which can provide better resolution. Based on the analysis of waveform and centroid frequency attributes for both polarizations, the cracks with varying widths and millimeter scale cracks can be identified in the "VV" and "HH" polarization profiles, respectively.

The proposed method is effective for identifying cracks, but further improvements are needed to make it suitable for extracting actual cracks, especially those with irregular orientations. We will enhance the experimental setup and incorporate full-polarization measurement or survey in future research to better align with real-world applications.

Author Contributions: Conceptualization, X.Z. and X.F.; methodology and scripts coding, X.Z. and J.P.; validation, X.H. and X.S.; formal analysis, X.Z.; investigation, C.C. and X.S.; resources and data curation, X.Z.; writing—original draft preparation, X.Z. and J.P.; writing—review and editing, X.Z. and Z.S.; visualization, J.P.; supervision and project administration, X.Z. and X.F.; funding acquisition. All authors have read and agreed to the published version of the manuscript.

Funding: This research is also funded by Scientific Research Programs granted by Jilin Provincial Department of science and technology, China (Grant No. 20240101046JC) and the National Natural Science Foundation of China (Grant No. 42004129). Changle Chen is funded by the Scientific Research Programs granted by Jilin Provincial Department of science and technology, China (Grant No. 20200201045JC).

Data Availability Statement: The data are available on request from the authors.

Acknowledgments: We thank the three anonymous reviewers for the time and effort in revision.

Conflicts of Interest: X.H. was employed by the company Jiangxi Transportation Engineering Group Ltd. The remaining authors declare that the research was conducted in the absence of any commercial or financial relationships that could be construed as a potential conflict of interest.

References

1. Grandjean, G.; Paillou, P.; Dubois-Fernandez, P.; August-Bernex, T.; Baghdadi, N.N.; Achache, J. Subsurface structures detection by combining L-band polarimetric SAR and GPR data: Example of the Pyla Dune (France). *IEEE. Trans. Geosci. Remote* **2001**, *39*, 1245–1258. [CrossRef]
2. Gross, R.; Green, A.G.; Horstmeyer, H.; Begg, J.H. Location and geometry of the Wellington Fault (New Zealand) defined by detailed three-dimensional georadar data. *J. Geophys. Res. Solid. Earth* **2004**, *109*, B05401. [CrossRef]
3. Jol, H.M. *Ground Penetrating Radar Theory and Applications*; Elsevier: Amsterdam, The Netherlands, 2009. [CrossRef]
4. He, R.; Nantung, T.; Olek, J.; Lu, N. Field study of the dielectric constant of concrete: A parameter less sensitive to environmental variations than electrical resistivity. *J. Build. Eng.* **2023**, *74*, 106938. [CrossRef]

5. Xie, L.Y.; Xia, Z.H.; Xue, S.T.; Fu, X.L. Detection of setting time during cement hydration using ground penetrating radar. *J. Build. Eng.* **2022**, *60*, 105166. [CrossRef]
6. Klewe, T.; Strangfeld, C.; Kruschwitz, S. Review of moisture measurements in civil engineering with ground penetrating radar—Applied methods and signal features. *Constr. Build. Mater.* **2021**, *278*, 122250. [CrossRef]
7. De Domenico, D.; Campo, D.; Teramo, A. FDTD modelling in high-resolution 2D and 3D GPR surveys on a reinforced concrete column in a double wall of hollow bricks. *Near Surf. Geophys.* **2012**, *11*, 29–40. [CrossRef]
8. Negri, S.; Aiello, M.A. High—Resolution GPR survey for masonry wall diagnostics. *J. Build. Eng.* **2021**, *33*, 101817. [CrossRef]
9. Arosio, D.; Hojat, A.; Munda, S.; Zanzi, L. High-Frequency GPR Investigations in Saint Vigilius Cathedral, Trento. In Proceedings of the 24th European Meeting of Environmental and Engineering Geophysics, Porto, Portugal, 9–12 September 2018; pp. 1–5.
10. Orlando, L. Detecting steel rods and micro-piles: A case history in a civil engineering application. *J. Appl. Geophys.* **2012**, *81*, 130–138. [CrossRef]
11. Rucka, M.; Lachowicz, J.; Zielinska, M. GPR investigation of the strengthening system of a historic masonry tower. *J. Appl. Geophys.* **2016**, *131*, 94–102. [CrossRef]
12. Cabaleiro, M.; Lindenbergh, R.; Gard, W.F.; Arias, P.; van de Kuilen, J.W.G. Algorithm for automatic detection and analysis of cracks in timber beams from LiDAR data. *Constr. Build. Mater.* **2017**, *130*, 41–53. [CrossRef]
13. Khamzin, A.K.; Varnavina, A.V.; Torgashov, E.V.; Anderson, N.L.; Sneed, L.H. Utilization of air-launched ground penetrating radar (GPR) for pavement condition assessment. *Constr. Build. Mater.* **2017**, *141*, 130–139. [CrossRef]
14. Saarenketo, T.; Scullion, T. Road evaluation with ground penetrating radar. *J. Appl. Geophys.* **2000**, *43*, 119–138. [CrossRef]
15. Wang, S.; Al-Qadi, I.L.; Cao, Q. Factors Impacting Monitoring Asphalt Pavement Density by Ground Penetrating Radar. *NDT E Int.* **2020**, *115*, 102296. [CrossRef]
16. Hui, V.H.Y.; Dérobert, X.; Lai, W.W.L. A study of artificial debond pavement under controlled traffic by Ground Penetrating Radar. *J. Appl. Geophys.* **2022**, *204*, 104722. [CrossRef]
17. Golewski, G.L. Evaluation of fracture processes under shear with the use of DIC technique in fly ash concrete and accurate measurement of crack path lengths with the use of a new crack tip tracking method. *Measurement* **2021**, *181*, 109632. [CrossRef]
18. Rasol, M.A.; Pérez-Gracia, V.; Fernandes, F.M.; Pais, J.C.; Santos-Assunçao, S.; Santos, C.; Sossa, V. GPR laboratory tests and numerical models to characterize cracks in cement concrete specimens, exemplifying damage in rigid pavement. *Measurement* **2020**, *158*, 107662. [CrossRef]
19. Zeng, H. Geologic significance of anomalous instantaneous frequency. *Geophysics* **2010**, *75*, P23–P30. [CrossRef]
20. Stockwell, R.G.; Mansinha, L.; Lowe, R.P. Localization of the Complex Spectrum: The S Transform. *IEEE Trans. Signal Process.* **1996**, *44*, 998–1001. [CrossRef]
21. Pinnegar, C.R.; Mansinha, L. The S-transform with windows of arbitrary and varying shape. *Geophysics* **2003**, *68*, 381–385. [CrossRef]
22. Li, D.; Castagna, J.; Goloshubin, G. Investigation of generalized S-transform analysis windows for time-frequency analysis of seismic reflection data. *Geophysics* **2016**, *81*, V235–V247. [CrossRef]
23. Liu, L.; Lane, J.W.; Quan, Y. Radar attenuation tomography using the centroid frequency downshift method. *J. Appl. Geophys.* **1998**, *40*, 105–116. [CrossRef]
24. Sattari, H. High-resolution seismic complex trace analysis by adaptive fast sparse S-transform. *Geophysics* **2017**, *82*, V51–V67. [CrossRef]
25. Quan, Y.; Harris, J.M. Seismic attenuation tomography using the frequency shift method. *Geophysics* **1997**, *62*, 895–905. [CrossRef]
26. Zhou, H.; Feng, X.; Zhou, B.; Dong, Z.; Fang, G.; Zeng, Z.; Liu, C.; Li, Y.; Lu, W. Polarized Orientation Calibration and Processing Strategies for Tianwen-1 Full-Polarimetric Mars Rover Penetrating Radar Data. *IEEE. Trans. Geosci. Remote* **2022**, *60*, 1–14. [CrossRef]
27. Dong, Z.; Feng, X.; Zhou, H.; Zhang, M.; Liu, Q.; An, Y.; Zhang, Y.; Yang, J.; Liang, W.; Yu, Y.; et al. Super-Resolution Detection of Millimeter-Scale Fractures with Fluid Flow Using Time-Lapse Full-Polarimetric GPR and Anisotropy Analysis. *IEEE. Trans. Geosci. Remote* **2024**, *62*, 1–16. [CrossRef]
28. Zhao, J.-G.; Sato, M. Radar Polarimetry Analysis Applied to Single-Hole Fully Polarimetric Borehole Radar. *IEEE. Trans. Geosci. Remote* **2006**, *44*, 3547–3554. [CrossRef]
29. Sassen, D.S.; Everett, M.E. 3D polarimetric GPR coherency attributes and full-waveform inversion of transmission data for characterizing fractured rock. *Geophysics* **2009**, *74*, J23–J34. [CrossRef]
30. Zhao, J.G.; Sato, M. A Fully Polarimetric Bobrehole Radar Based Numerical Modelling: Fully Polarimetric Response to Synthetic Fractures and "Fluid Substitution". In Proceedings of the 2010 IEEE International Geoscience and Remote Sensing Symposium, Honolulu, HI, USA, 25–30 July 2010.
31. Yu, Y.; Feng, X.; Liu, C.; Lu, Q.; Hu, N.; Ren, Q.; Nilot, E.; You, Z.; Liang, W.; Fang, Y. Radar Polarimetry Analysis Applied to Fully Polarimetric Ground Penetrating Radar. In Proceedings of the 15th International Conference on Ground Penetrating Radar—GPR, Brussels, Belgium, 30 June 2014–4 July 2014.
32. Pinnegar, C.R.; Mansinha, L. Time-local Fourier analysis with a scalable, phase-modulated analyzing function: The S-transform with a complex window. *Signal. Process* **2004**, *84*, 1167–1176. [CrossRef]
33. Zhang, X.; Song, Z.; Li, B.; Feng, X.; Zhou, J.; Yu, Y.; Hu, X. The LPR Instantaneous Centroid Frequency Attribute Based on the 1D Higher-Order Differential Energy Operator. *Remote. Sens.* **2023**, *15*, 5305. [CrossRef]

34. Zhang, X.; Hu, X.; Qiu, Z.; Feng, X.; Qin, Y. Extraction of the GPR instantaneous centroid frequency based on the envelope derivative operator and ICEEMDAN. *Remote Sens. Lett.* **2023**, *14*, 469–478. [CrossRef]
35. Li, J.; Zeng, Z.; Liu, C.; Huai, N.; Wang, K. A Study on Lunar Regolith Quantitative Random Model and Lunar Penetrating Radar Parameter Inversion. *IEEE Geosci. Remote Sens. Lett.* **2017**, *14*, 1953–1957. [CrossRef]
36. Zhang, X.B.; Liu, C.; Feng, X.; Li, B.N.; Li, K.X.; You, Q. The attenuated Ricker wavelet basis for seismic trace decomposition and attenuation analysis. *Geophys. Prospect.* **2020**, *68*, 371–381. [CrossRef]
37. Zhukov, A.D.; Ter-Zakaryan, K.A.; Semenov, V.S. Insulation systems with the expanded polyethylene application. *IFAC-Pap.* **2018**, *51*, 803–807. [CrossRef]
38. Zhang, T.; Yuan, J.; Pang, H.; Huang, Z.; Guo, Y.; Wei, J.; Yu, Q. UHPC-XPS insulation composite board reinforced by glass fiber mesh: Effect of structural design on the heat transfer, mechanical properties and impact resistance. *J. Build. Eng.* **2023**, *75*, 106935. [CrossRef]
39. Brown, S.; Caprihan, A.; Hardy, R. Experimental observation of fluid flow channels in a single fracture. *J. Geophys. Res. Solid Earth* **1998**, *103*, 5125–5132. [CrossRef]
40. Qian, Z.; Schlangen, E.; Ye, G.; van Breugel, K. Modeling Framework for Fracture in Multiscale Cement-Based Material Structures. *Materials* **2017**, *10*, 587. [CrossRef] [PubMed]
41. Tsoflias, G.P.; Van Gestel, J.P.; Stoffa, P.L.; Blankenship, D.D.; Sen, M. Vertical fracture detection by exploiting the polarization properties of ground-penetrating radar signals. *Geophysics* **2004**, *69*, 803–810. [CrossRef]
42. Radzevicius, S.J.; Daniels, J.J. Ground penetrating radar polarization and scattering from cylinders. *J. Appl. Geophys.* **2000**, *45*, 111–125. [CrossRef]

Disclaimer/Publisher's Note: The statements, opinions and data contained in all publications are solely those of the individual author(s) and contributor(s) and not of MDPI and/or the editor(s). MDPI and/or the editor(s) disclaim responsibility for any injury to people or property resulting from any ideas, methods, instructions or products referred to in the content.